Research Article Vol. 13, No. 4 / 1 Apr 2022 / Biomedical Optics Express 2467
Biomedical Optics EXPRESS

Co-localized line-field confocal optical coherence tomography and confocal Raman microspectroscopy for three-dimensional high-resolution morphological and molecular characterization of skin tissues *ex vivo*

LÉNA WASZCZUK,[1,2,*] JONAS OGIEN,[2] JEAN-LUC PERROT,[3] AND ARNAUD DUBOIS[1,2]

[1] *Université Paris-Saclay, Institut d'Optique Graduate School, CNRS, Laboratoire Charles Fabry, Palaiseau 91127, France*
[2] *DAMAE Medical, Paris 75013, France*
[3] *University Hospital of Saint-Etienne, Department of Dermatology, 42055 Saint-Etienne, France*
[*] *lena.waszczuk@universite-paris-saclay.fr*

Abstract: Line-field confocal optical coherence tomography (LC-OCT) is an optical modality that provides three-dimensional (3D) images of the skin at cellular resolution. Confocal Raman microspectroscopy (CRM) is a label-free optical technique that can provide point measurement of the molecular content of the skin. This work presents a method to co-localize LC-OCT and CRM acquisitions for morpho-molecular analysis of *ex vivo* skin tissues at cellular level. The co-localization method allows acquisition of Raman spectra at specific locations in a sample identified from a 3D LC-OCT image, with an accuracy of ± 20 µm. The method was applied to the characterization of tattooed skin biopsies with adverse tattoo reactions. LC-OCT images allowed to target specific regions in the biopsies where the presence of tattoo ink was revealed by detection of the Raman signature of ink pigments. Micrometer-sized foreign bodies of various materials as well as inflammatory cells were also identified within the biopsies. From these results, we demonstrate the value of the LC-OCT-CRM co-localization method and its potential for future *ex vivo* analysis of suspicious skin lesions.

1. Introduction

Line-field confocal optical coherence tomography (LC-OCT) is a recently invented imaging technique designed for *in vivo* skin imaging, which combines the principles and advantages of two imaging modalities, optical coherence tomography (OCT) and reflectance confocal microscopy (RCM) with line illumination and detection [1–4]. LC-OCT generates two-dimensional (2D) vertical and horizontal images as well as three-dimensional (3D) images of the skin at cellular resolution [5]. LC-OCT provides images of the superficial layers of the skin, with a high level of structural details and a penetration down to 500 µm. The potential of LC-OCT in dermatology was demonstrated by numerous studies, both for healthy skin characterization [6–8] and for identification and characterization of various skin pathologies *in vivo*, such as basal cell carcinoma and its different subtypes [9,10], squamous cell carcinoma [11] and actinic keratosis [11,12]. LC-OCT images provide morphological information, originating from heterogeneities of the refractive index of skin components. LC-OCT images, although of high resolution, are sometimes complex to interpret in the case of pathologies with ambiguous morphological features or early-stage pathologies with only few structural changes. Other optical modalities based on spectroscopy could provide complementary information on the biochemical composition of the skin, allowing to address such cases.

#450993 https://doi.org/10.1364/BOE.450993
Journal © 2022 Received 10 Dec 2021; revised 22 Feb 2022; accepted 2 Mar 2022; published 25 Mar 2022

Biomedical Optics EXPRESS

Raman spectroscopy is a label-free technique that probes vibrations of chemical bonds [13]. It provides a spectrum determined by the molecules constituting the sample being analyzed, often referred to as the sample molecular fingerprint. Confocal Raman microspectroscopy (CRM) provides in-depth point-wise measurements of the molecular composition, rejecting Raman scattering from out of focus regions. CRM is a popular technique in the field of dermocosmetics where it is used to study the effects of cosmetic formulations on the skin [14–16], to monitor the penetration of cosmetic actives into the skin [17–19] or to study skin chronologic- and photo-aging [20,21]. CRM is also of great interest in the field of onco-dermatology, for instance during Mohs surgery [22,23], and for *ex vivo* [24–26] and *in vivo* skin cancer diagnosis [27]. CRM is also used in skin cancer research for *in vitro* studies on cancer cells [28–30] or investigation of molecular skin cancer markers [31–33]. CRM can also be applied in dermatology to the characterization of tattoos. Obtained by inserting pigment micro- or nano-particles into the dermis using needles, tattoos can cause various cutaneous reactions, such as non-allergic inflammatory reactions and allergic reactions to certain pigments and metal particles contained in the tattoo ink. CRM was used to characterize *ex vivo* and *in vivo* tattoo inks of different colors [34–36] and identify tattoo inks causing skin reactions [37,38]. CRM is also capable of providing ink composition and one-dimensional (1D) depth distribution down to 400 μm [36], which could be of interest for laser removal. However, CRM is usually limited to point measurements, which can make the use in a clinical setting fastidious if no morphological image is available to guide Raman spectra acquisition.

Correlation of morphological and biochemical findings would yield a better characterization of the skin and its pathologies. Several research groups have already developed systems combining imaging modalities such as OCT and RCM with Raman spectroscopy for dermatological applications. Bimodal OCT-Raman systems were mainly developed for screening and diagnosis of skin cancers *in vivo* [39–42]. These systems were designed to probe large areas of skin, with limited spatial resolution (> 3 μm for OCT, > 100 μm for Raman spectroscopy) and large fields of view (several mm) [40–44]. As a result, acquisition times are relatively short (< 30s for the acquisition of a Raman spectrum) which allows the use in clinical settings. OCT provides imaging guidance of Raman spectroscopy, which greatly facilitates Raman spectra acquisitions in regions of interest. On the other hand, the Raman measurements bring complementary information to the morphological images provided by OCT. Nevertheless, by probing such large volumes of skin over several millimeters, the information of interest (*e.g.*, a pathological area of skin) could be obscured by the surrounding healthy tissue. It is therefore interesting to probe smaller volumes to better isolate the structures of interest. Coupled RCM-CRM systems provide combination of morphological and biochemical information at the cellular level since both modalities operate at a micrometric scale. CRM sub-systems provide biochemical composition within the RCM image, from point measurements [45,46] to local measurements within regions of interest (ROIs) selected in the RCM image, allowing faster Raman acquisition [47,48]. Unlike coupled OCT-Raman systems, RCM-CRM systems allow precise targeting of micro-structures in the skin. However, contrary to OCT, RCM is limited to providing horizontal images, which can complexify visualization and targeting of depth-resolved structures. Vertical images can be reconstructed from 3D images obtained from a stack of horizontal RCM images. However, they are not obtained in real time and have a lower resolution than horizontal images, so they do not allow easy identification of in-depth micro-structures. Additionally, such combined instruments require compromises on the performance of both modalities since they share some of the optical elements but have different technical specifications. Another approach to combine the imaging and spectroscopic modalities is to perform co-localized acquisitions, using two separate systems. A set-up for *ex vivo* co-registration of OCT and Raman acquisitions was previously reported in the literature [49,50]. Based on a translation of the sample between the two separate systems using an XY motorized stage, the method consists in scanning a whole biopsy with both modalities

Biomedical Optics EXPRESS

using pre-defined sampling points. This approach allows combination of 3D OCT images and 2D en face Raman maps. However, the two systems have non-cellular resolution and provide information at different scales: the OCT device provides 3D images with a limited resolution (28 µm lateral resolution, 12 µm axial resolution) which does not allow cellular targeting; the Raman system was designed to probe large areas (lateral spot size of 100 µm) of *ex vivo* tissue compared to the OCT resolution and provides 2D Raman maps, which allows fast Raman acquisitions but does not allow local Raman analysis nor precise 3D location within the OCT image.

In this paper, we propose to combine LC-OCT and CRM for co-localized acquisitions. The technique allows acquisition of Raman spectra of specific cellular-level structures within a sample, based on their morphological features identified from 3D LC-OCT images. In order to demonstrate the potential of our LC-OCT-CRM co-localization technique, we applied it to the analysis of tattooed skin biopsies with adverse tattoo reactions. Combination of LC-OCT and CRM allows to locate tattoo pigments in the dermis, to identify the tattoo ink used and to better characterize the reaction, which can contribute to improvement of clinical management of such tattoo reactions.

2. Materials and methods

2.1. LC-OCT device

The LC-OCT device used is a custom-built system designed for *ex vivo* applications, schematically represented in Fig. 1. It is similar to the system designed for *in vivo* applications, described in detail in [1,2,4,5], except that the sample is contained in a sample holder and a path for providing a color image of the surface of the sample was added to the device.

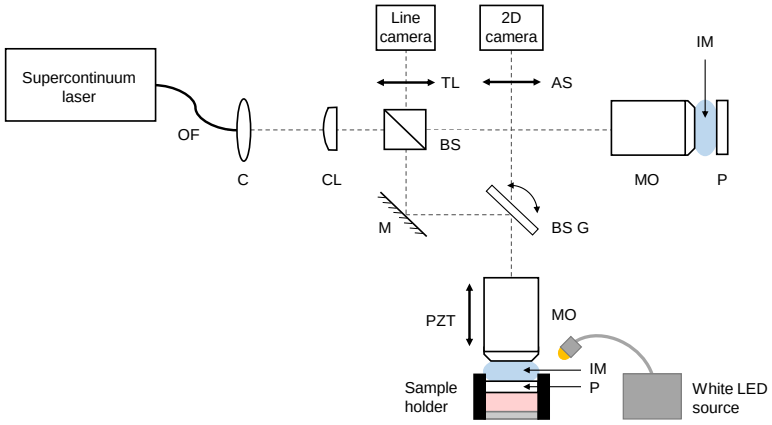

Fig. 1. Schematic of the LC-OCT system dedicated to *ex vivo* imaging, combining a LC-OCT imaging path and a surface imaging path. OF: optical fiber; C: collimator; CL: cylindrical lens; BS: beamsplitter; M: mirror; BS G: beamsplitter mounted on galvanometer scanner; MO: microscope objective; PZT: piezoelectric translation stage; TL: tube lens; AS: afocal system for surface imaging; P: CaF_2 plate; IM: immersion medium.

The sample holder, illustrated in Fig. 2, is placed under the microscope objective of the sample arm. The top of the sample holder is covered with a 1 mm thick plate made of Raman-grade calcium fluoride (CaF_2) (Crystran Ltd, Poole, UK). An identical plate is introduced in the reference arm to ensure identical optical dispersion in both arms of the interferometer. Raman-grade CaF_2 was chosen since its Raman signature is composed of a single Raman peak at 321 cm^{-1}, thus minimizing background Raman signal superimposed on the Raman spectra of skin

Biomedical Optics EXPRESS

samples. Optical contact between the CaF_2 window and the skin sample is obtained using a very thin layer of paraffin oil. The sample is placed in the sample holder with its surface directed towards the CaF_2 window. A glass plate is added under the sample. Its position is adjusted with a retaining ring to gently press the sample against the top window and prevent any displacement of the sample during the experiments. Silicone oil is added on top of the sample holder as an immersion medium. Silicone oil has a refractive index of 1.4 close to the refractive index of skin, which ensures superimposition of the coherence plane and the focal plane of the objective during the depth scan and thereby maintains optimal axial resolution at all depths [2,51]. The *ex vivo* LC-OCT prototype provides real-time 2D vertical and horizontal images covering a field of view of 1.2 mm × 0.5 mm ($x \times z$ for vertical imaging mode and $x \times y$ for horizontal imaging mode). 3D LC-OCT images can also be acquired, with a quasi-isotropic resolution of ~ 1 µm, and a field of view of 1.2 mm × 0.5 mm × 0.5 mm ($x \times y \times z$).

In addition to in-depth images, the LC-OCT device provides a color image of the skin surface. This image is acquired along a second optical path, also shown in Fig. 1. A white LED source (8W LED Dual Gooseneck Spot Light, Omano, USA) illuminates the surface of the sample. Light reflected from the surface is collected by the microscope objective of the LC-OCT device, allowing the surface image and LC-OCT image to be acquired simultaneously. The optical paths for those two images are separated using a beamsplitter (BSX11R, Thorlabs, USA) placed on the galvanometer used for lateral line-scanning (6210H single-axis galvanometer scanner, Cambridge Technology, USA). A custom-built afocal system then guides the light of the surface image optical path to a 2D color camera equipped with a micro-lens (uEye XS, IDS Imaging Development Systems GmbH, Germany), which focuses light on the camera sensor to obtain a 2D color image of the skin surface. The surface image provided by the LC-OCT device has a spatial resolution of 5 µm (versus a spatial resolution of ~ 1 µm for the in-depth 3D LC-OCT images) and covers a field of view of 2.5 mm in diameter that includes the LC-OCT field of view. The position of the LC-OCT acquisition is represented by a graphical marker on the surface image. The surface image helps positioning the sample with respect to the LC-OCT device and to correlate LC-OCT in-depth findings with surface examination of the skin.

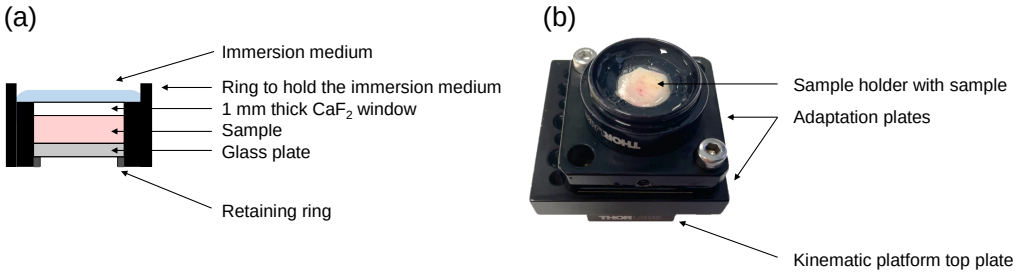

Fig. 2. (a) Schematic view of the sample holder dedicated to co-localization experiments. The top of the sample holder is covered with a 1 mm thick Raman-grade CaF_2 window. The skin sample is gently pressed against the CaF_2 using a glass plate positioned below the skin sample and moved upwards using a retaining ring. Immersion medium is added on top of the sample holder. (b) Picture of the sample holder.

2.2. CRM device

A schematic of the CRM device is given in Fig. 3. It is an in-house developed set-up, using a continuous-wave (CW) laser emitting at 785 nm (Micron Cheetah, Sacher Lasertechnik GmbH, Germany). The 785 nm Raman excitation wavelength was chosen as a compromise to collect a sufficient amount of Raman signal, while minimizing the amount of autofluorescence that

Biomedical Optics EXPRESS

superimposes on the Raman signal [52,53]. The use of a wavelength in the near infrared also allows to obtain an optimal penetration owing to the minimal absorption of biological tissues in this spectral domain (known as the tissue therapeutic window) [54,55]. The excitation beam is brought to the CRM set-up using a 5 µm-core diameter, 0.1 NA, polarization-maintaining optical fiber (PMJ-3A3A-850-5/125-3-1.5-1, OZ Optics, Canada), and collimated using an off-axis parabolic mirror (RC08APC-P01, Thorlabs, USA) placed at the output of the fiber. A sharp band-pass filter (785 nm MaxLine laser clean-up filter, Semrock Inc., USA) removes potential parasitic wavelengths. The beam is focused on the sample using a 40x 0.8-NA water-immersion microscope objective (LUMPLFLN40XW, Olympus, Japan). The Raman signal is collected by the same objective and separated from the excitation beam using a dichroic beamsplitter (785 nm RazorEdge Dichroic laser beamsplitter, Semrock Inc., USA). A long-pass edge filter (785 nm RazorEdge ultrasteep long-pass edge filter, Semrock Inc., USA) eliminates the detection of residual excitation. The Raman signal is focused into a 105 µm-core diameter, 0.22-NA, multimode optical fiber (M18L01, Thorlabs, USA) using an off-axis parabolic mirror (RC08FC-P01, Thorlabs, USA). The optical fiber both guides the Raman signal to a spectrometer and serves as a confocal aperture. The spectrometer is equipped with gold-coated mirrors and a back-thinned FFT-CCD detector (QE Pro-Raman+, Ocean Insight, USA) and has a spectral resolution of 11 cm^{-1}.

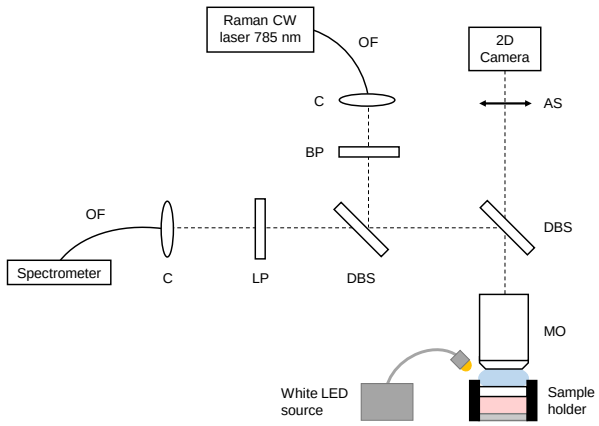

Fig. 3. Schematic of the CRM custom set-up, combining a Raman spectroscopy path and a surface imaging path. OF: optical fiber; C: collimator (off-axis parabolic mirror); BP: band-pass filter; LP: long-pass filter; DBS: dichroic beamsplitter; MO: microscope objective; AS: afocal system.

The diameter of the collection fiber defines the axial extension of the probed Raman volume. A diameter of 105 µm, coupled to a 40x microscope objective, provides a resolution of ~ 1 µm × 1 µm × 30 µm ($x \times y \times z$). This value was chosen as a trade-off to collect a sufficient amount of Raman signal, while allowing accurate location of the depth probed with the CRM system within an LC-OCT image. Water is used as immersion medium in the CRM device in order to minimize optical aberrations that could distort and enlarge the probed volume.

As in the LC-OCT device, an optical path providing a surface image of the sample was integrated into the CRM device. This path uses an identical white LED source (8W LED Dual Gooseneck Spot Light, Omano, USA) to illuminate the sample. Light reflected by the surface of the sample is collected by the same microscope objective used for CRM and separated from the Raman excitation and Raman signal using a dichroic beamsplitter (750 nm edge BrightLine single-edge standard epi-fluorescence short-pass dichroic beamsplitter, Semrock Inc., USA).

Biomedical Optics EXPRESS

Using an afocal system similar to the one used in the LC-OCT device, the surface image is projected onto a 2D camera equipped with a micro-lens (uEye XS, IDS Imaging Development Systems GmbH, Obersulm, Germany). The surface image covers a field of view of 1.4 mm in diameter and has a spatial resolution of 3 µm, as illustrated in Fig. 4.

The output power on the sample was set to 50 mW. Raman spectra were recorded in a range from 0 to 3000 cm^{-1}, with a 10s integration time and a 6-fold accumulation. All Raman spectra were slightly smoothed using a moving average filter and subtracted from background autofluorescence by fitting a fifth-order polynomial function on the acquired spectra.

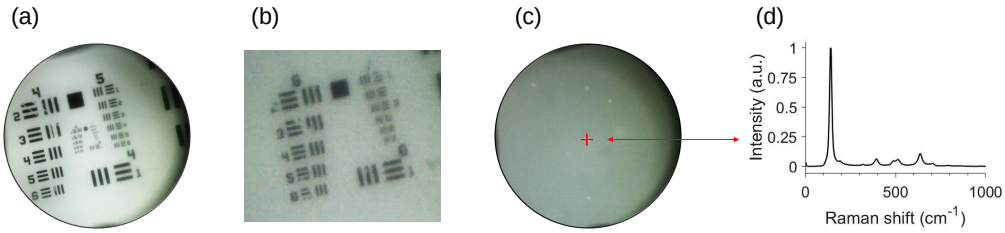

Fig. 4. Color surface image provided by the CRM set-up. (a) Surface image of a 1951 USAF resolution target. The surface image covers a field of view of 1.4 mm in diameter. (b) Zoom of surface image in (a), showing a 3 µm resolution. (c) Surface image of a polydimethylsiloxane phantom including titanium dioxide (TiO_2) beads. The red cross represents the lateral location of the CRM focal point within the surface image and here targets a TiO_2 bead. (d) Raman spectrum associated to the TiO_2 bead targeted in (c), showing Raman peaks assigned to the anatase form of TiO_2 at 143, 396, 512, 521 and 639 cm^{-1} [56].

2.3. *Co-localization set-up and principle*

A schematic representation of the co-localization set-up is given in Fig. 5. Identical XYZ translation stages are placed under the microscope objective of the LC-OCT sample arm and under the CRM objective. To perform co-localization experiments, the sample holder is first placed on the translation stage of the LC-OCT device. The sample can thus be positioned with respect to the LC-OCT objective. Thanks to both real-time 2D horizontal and vertical imaging, ROIs in the 3D sample can be easily and quickly identified. Once a ROI is identified in the sample, a 3D LC-OCT image of this ROI is acquired, and the corresponding XYZ coordinates on the translation stage are recorded. Specific POIs to be analyzed with CRM are selected within the 3D image. The sample holder is then manually moved to the CRM stage. Based on a calibration performed prior to experiments, the XYZ coordinates of the CRM stage allowing to position each selected POI at the CRM focal point are computed. For each POI, the stage is then moved to the corresponding computed coordinates, and a Raman spectrum is acquired. Pictures of the co-localization set-up are shown in Fig. S1 of Supplement 1.

Calibration aims at finding the transfer relation between the coordinates of any POI in a 3D LC-OCT image (acquired for given XYZ coordinates on the LC-OCT stage) and the XYZ coordinates on the CRM stage that makes this POI positioned at the CRM focal point. The transfer relation can be expressed by a combination of a rotation matrix and a translation matrix. Calibration is performed using a calibration sample. The calibration sample is composed of a matrix of polydimethylsiloxane (Sylgard 184 Silicone Elastomer, Dow Corning, USA) containing titanium dioxide (TiO_2) beads (anatase form, Sigma-Aldrich Corporation, USA). This sample is well suited both for Raman spectroscopy and LC-OCT imaging since PDMS and TiO_2 have different Raman signatures and different refractive indexes ($n_{PDMS} = 1.40$, $n_{TiO_2} = 2.52$), leading to high image contrast.

Biomedical Optics EXPRESS

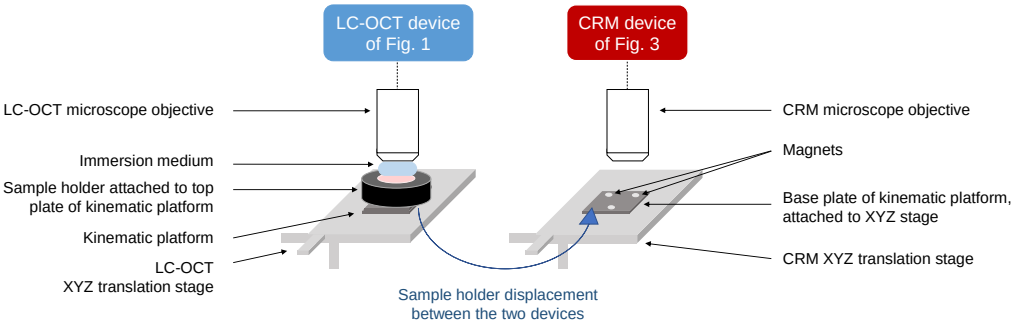

Fig. 5. Schematic view of the co-localization set-up. The two devices (LC-OCT and CRM) are independent. XYZ translation stages are placed under the microscope objective of each device. The sample is placed in a sample holder that can be placed on the XYZ translation stage of each device. The use of a magnetic kinematic platform allows to position the sample holder with high repeatability.

The calibration process is schematically described in Fig. S2 of Supplement 1. Calibration is achieved by identifying TiO_2 beads in the calibration sample with LC-OCT, and then placing those same beads at the focal point of the CRM device. In order to target the same bead with LC-OCT and CRM for this procedure, the surface images are used to identify specific beads. As shown in Fig. 4, TiO_2 beads are visible in the surface images nevertheless they all appear similar. Ink dots were therefore added to the surface of the calibration sample, so that the beads could be differentiated from each other based on their position relative to the ink dots visible in the surface images of the LC-OCT device and the CRM device (see Fig. S2 of Supplement 1). The CRM can then be guided to place at its focal point the same TiO_2 bead previously identified with LC-OCT. For each TiO_2 bead identified with LC-OCT and retrieved with CRM, the XYZ coordinates on the LC-OCT stage and on the CRM stage are recorded. During this procedure, the beads are always positioned at the same image coordinates within the LC-OCT image, referred to as the (0,0,0) image coordinates. By targeting multiple TiO_2 beads, LC-OCT/CRM pairs of XYZ stage coordinates are obtained. The transfer relation between the (0,0,0) image coordinates of any LC-OCT image and the corresponding XYZ coordinates of the CRM stage can then be established. From the transfer relation, the XYZ coordinates of the CRM stage corresponding to any POI within the LC-OCT image can be obtained by adding an offset to the CRM stage corresponding to the image coordinates of the POI. Once the calibration is done, a skin sample is placed in the sample holder, and co-localized LC-OCT and CRM acquisitions are performed using only the XYZ coordinates of the LC-OCT and CRM stages and the transfer relation between the two.

For calibration to be possible, the calibration sample and later the skin sample must be fixed in the sample holder when switched from the LC-OCT stage to the CRM stage. Sample displacements are prevented by gently compressing the sample between the two glass slides of the sample holder, as previously described. Once done, the calibration must be preserved during acquisitions on skin samples. This requires that the sample holder is repositioned on each stage at exactly the same position as during calibration operations. If not the case, the transfer relation between the coordinates of the two stages is affected. However, the skin sample can be positioned in the sample holder without any particular precaution since it remains fixed in the sample holder when moved from the LC-OCT stage to the CRM stage. To ensure identical repositioning of the sample holder on each stage as during calibration, a kinematic platform (KB25/M, Thorlabs, USA) is used. This platform is composed of two plates held together by magnets and precisely positioned one in relation to the other thanks to a system of balls and grooves. The base plate is

Biomedical Optics EXPRESS

attached to each XYZ stage, while the top plate is attached to the sample holder. The kinematic platform allows sample holder repositioning with a high repeatability (≤ 3 µm). With the set-up used, the accuracy of the co-localization is limited by the 10 µm pitch of the two XYZ translation stages used. The accuracy of the co-localization procedure was experimentally evaluated through a repeatability study: using the calibration sample, 10 TiO_2 beads at different XYZ positions in the calibration sample were imaged using LC-OCT. The calibration sample was then moved to the CRM stage, and for each bead identified in LC-OCT images, the corresponding coordinates to be reached on the CRM stage to target this bead with the CRM device were computed, using prior calibration. Using the surface image of the CRM device and the Raman signal of TiO_2, we quantified the positioning error, defined as the deviation between the theoretical XYZ coordinates of the CRM stage given by the calibration and the actual XYZ coordinates of the stage to effectively target the center of the bead with CRM. Experimental results are given in Table S1 of Supplement 1. The co-localization accuracy was considered as the maximum positioning error (worst case accuracy), *i.e.*, ± 20 µm in X/Y and ± 10 µm in Z, which allows combining morphological and biochemical information at the cellular scale.

A self-built desktop application dedicated to co-localization was designed, operating in a MATLAB environment (MATLAB R2020a, MathWorks, USA). Calibration data (*i.e.*, the transfer relation) is stored in the application. The graphical interface allows the user to upload a 3D LC-OCT image and its XYZ stage coordinates, and to select multiple POIs within this image using crosshairs. Based on initial calibration, the application computes the CRM stage coordinates associated to each POI.

2.4. Skin samples

Three biopsies of tattooed human skin were characterized by co-localized LC-OCT and CRM measurements. Biopsies were taken from patients who experienced adverse skin reactions and were provided by the Department of Dermatology of the University Hospital of Saint-Etienne (France). They included two biopsies of ink tattoos and a biopsy of a fulguration-induced tattoo. The biopsies were stored at -80°C and defrosted at ambient temperature a few minutes before co-localization experiments.

The first biopsy was taken from a 40-year-old patient who experienced a severe delayed reaction from red dye 8 months after tattoo execution. His case was previously reported in the literature [57]: the patient presented plaques within the red dye areas of his multicolored tattoo and was examined using dermoscopy, LC-OCT, high-frequency ultrasound (HFUS) and histology. Signs of inflammation with presence of inflammatory infiltrate and dilated vessels were pointed out by LC-OCT and HFUS images. A biopsy was taken within the red dye area where presence of B and T lymphocytes was revealed by immunohistochemical examination. This case is not isolated since several red pigments and metals (such as cadmium, mercury, nickel, iron) contained in red inks were reported in the literature as chronic sensitizers and allergens [37,58]. CRM could thus provide additional information such as identification of the tattoo ink and its specific compounds causing the reaction. CRM could also allow to better characterize the inflammatory reaction, similarly to immunohistochemistry which provides identification of inflammatory infiltrates, but without requiring any sample preparation.

The second biopsy was obtained from a 33-year-old patient who had nodules appear on his black tattoo 6 months after execution of the tattoo. A biopsy was performed and histological diagnosis concluded to sarcoidosis. Cases of tattoo-induced sarcoidosis have already been reported in the literature [59,60]. A study on tattoo reactions [61] revealed that black tattoos with papulo-nodular reactions may be markers of sarcoidosis. CRM could provide identification of the black pigment involved in the papulo-nodular reaction, which could help understanding underlying phenomena between tattooing and sarcoidosis development.

Biomedical Optics EXPRESS

The last biopsy was taken from a 45-year-old patient wearing a silver necklace and struck by lightning, a case previously reported in the literature [62]. The patient presented a pigmentation of the neck area and was examined using dermoscopy, RCM and LC-OCT. RCM and LC-OCT images revealed the presence of hyper-reflective roundish particles of about 20-40 μm in diameter in the dermis, suggesting that particles from the silver necklace deposited in the patient's dermis after melting of the necklace during the light strike. The LC-OCT-CRM co-localization will provide additional information on the chemical composition of these small bright particles spotted in the LC-OCT image, which may yield a better understanding of the melting phenomenon that occurred during the lightning strike.

3. Results and discussion

A 3D LC-OCT image of each biopsy was acquired, in which multiple POIs were targeted and analyzed using CRM. An example of 3D LC-OCT image is given in Fig. 6, with targeted POIs materialized by red ellipsoids. The ellipsoids represent the volume in which the Raman acquisition is included. The volume probed by CRM is ~ 1 μm × 1 μm × 30 μm ($x \times y \times z$), but the uncertainty of the co-localization procedure in X/Y is ± 20 μm and in Z ± 10 μm (included in the 30 μm axial extent), resulting in dimensions of 40 μm × 40 μm × 30 μm for the axes of the ellipsoids.

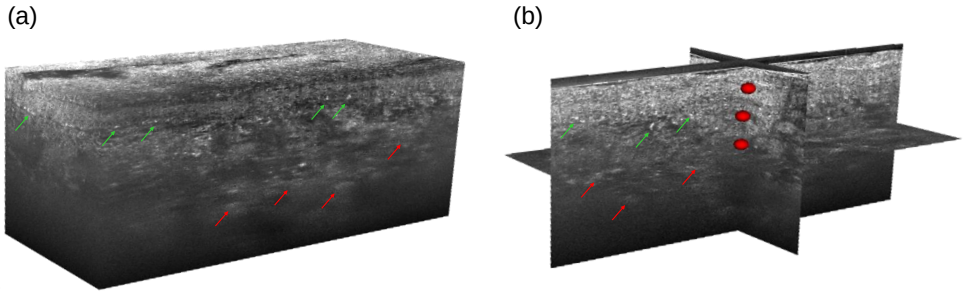

Fig. 6. (a) 3D LC-OCT image and (b) orthogonal views of a red-colored tattoo biopsy with multiple POIs materialized by red ellipsoids. Diffuse bright areas in the dermis can be observed in the LC-OCT image, depicted by red arrows. Hyper-reflective structures of about 10-40 μm in size can be noticed near the dermal-epidermal junction, pointed out by green arrows.

In the following, it should be noted that for interpretation of the Raman spectra, only peaks relevant for biochemical identification were selected, based on Raman data available in the literature. The selected peaks are depicted by arrows on Raman spectra in the following figures. Peaks that could not be precisely identified were not included. The selection is not exhaustive but is sufficient to demonstrate the potential and value of combining the morphological information provided by LC-OCT and the molecular information provided by CRM.

3.1. Biopsy 1: red-colored tattoo

Co-localization experiments were first carried out on the biopsy taken within the red dye area of a multicolored tattoo. Results are presented in Fig. 7. For better visualization, POIs are displayed on 2D horizontal and/or vertical images extracted from the 3D image. The LC-OCT image allows to distinguish the different superficial layers of the skin: the epidermis (E), including the stratum corneum (SC), and the dermis (D). Diffuse bright areas in the dermis can be observed in the LC-OCT image (depicted by red arrows in Fig. 6 and Fig. 7), suggesting the presence of

Biomedical Optics EXPRESS

tattoo ink in these areas. Moreover, hyper-reflective structures of about 10-40 μm in size can be noticed near the dermal-epidermal junction (green arrows in Fig. 6 and Fig. 7). Five POIs were targeted within the 3D LC-OCT image. POI 1 is located in the epidermis (E); POIs 2 and 4 were chosen in the dermis (D) at 200 μm and 185 μm depths respectively; POI 3 targets a hyper-reflective structure located near the dermal-epidermal junction (at 120 μm depth); POI 5 was chosen in the dermis at 305 μm depth, in a diffuse and brighter region compared to POI 4. Using the co-localization procedure, Raman spectra were acquired at each location. The spectrum acquired at POI 1 exhibits the Raman signature of the epidermis alone, with main typical Raman bands at 852, 895, 936, 1001, 1300-1350, 1443 and 1650 cm^{-1} [63] depicted by blue arrows. The spectrum of POI 1 shows no sign of tattoo ink, which could be expected since ink is conventionally injected directly in the dermis. The spectrum acquired at POI 2, located in the dermis and underneath POI 1, shows multiple sharp peaks above 1200 cm^{-1}, with major Raman shifts at 1239, 1284, 1360, 1422, 1486, 1550 and 1612 cm^{-1} depicted by red arrows. These peaks are characteristic of the molecular signature of a red tattoo ink. More precisely, according to red pigments already characterized in the literature with CRM, the spectrum is characteristic of an azo-based pigment [34,64]. Red azo pigments are organic pigments that were already reported to be involved in various cutaneous reactions in tattoos [58,65,66]. In particular, a case of delayed inflammatory reaction with signs of lichenoid dermatitis in a tattoo executed with a red azo pigment was reported [67]. The similarity with the biopsy of red dye tattoo reaction being studied here [57] suggests that the red pigment identified as azo-type may be implicated in the reaction. The Raman bands assigned to the ink are also clearly visible in the spectrum of POIs 4 and 5 (red arrows). Additional clear peaks around 585, 967, 1028 and 1194 cm^{-1} can also be noticed in the spectra of POIs 4 and 5. However, their identification is not clear and their absence in the spectrum of POI 2 has not been explained yet. One can notice that the Raman peaks of the red ink are more intense in POI 5 than POI 4, despite the fact that POI 5 is located much deeper. This finding can be correlated to observations made in the LC-OCT image since POI 5 is located in a brighter region of the dermis than POI 4. This result suggests that brighter areas contain a higher amount of tattoo ink.

POI 3 exhibits a different spectrum from the skin and ink, with a broad and intense peak centered around 565 cm^{-1} (green arrow) as well as peaks which are also visible in the spectrum of the red tattoo ink (red arrows). These sharp peaks are included in a broad band from 1200 to 1650 cm^{-1} (green bracket). The same spectrum was obtained for several other bright particles (pointed out by the green arrows on the LC-OCT horizontal image in Fig. 7). Several hypotheses were investigated to interpret this spectrum. The bright particles could be contained in the tattoo ink such as aggregates of specific pigments or metal particles, as mentioned before. A second hypothesis suggests that the bright particles are biological cells such as inflammatory cells activated in reaction to tattooing. These inflammatory reactions involve various inflammatory cells, including lymphocytes, which were previously detected within the biopsy by immunohistochemistry [57]. Reactions in tattoos can also involve macrophages, which are white blood cells having the capacity to ingest and destroy foreign particles. Several publications [68–70] studying tattoos with RCM have shown their presence near the dermal-epidermal junction and in the dermis of tattooed skin, as part of an inflammatory reaction. These macrophages engulf ink pigment and appear as groups of small hyper-reflective particles, with irregular or spindle shapes. These findings reported with RCM match the morphological features of the bright particles observed with LC-OCT. However, very few publications have characterized macrophages with Raman spectroscopy. Tetard *et al.* [71,72] reported the Raman spectrum of macrophages, which interestingly shows a peak centered around 570 cm^{-1} as well as a broad band from ~1200 to 1650 cm^{-1}. The additional sharp peaks also found in tattoo ink (red arrows) may be explained by tattoo pigment engulfment by macrophages. Both morphological and molecular information thus converge

Biomedical Optics EXPRESS

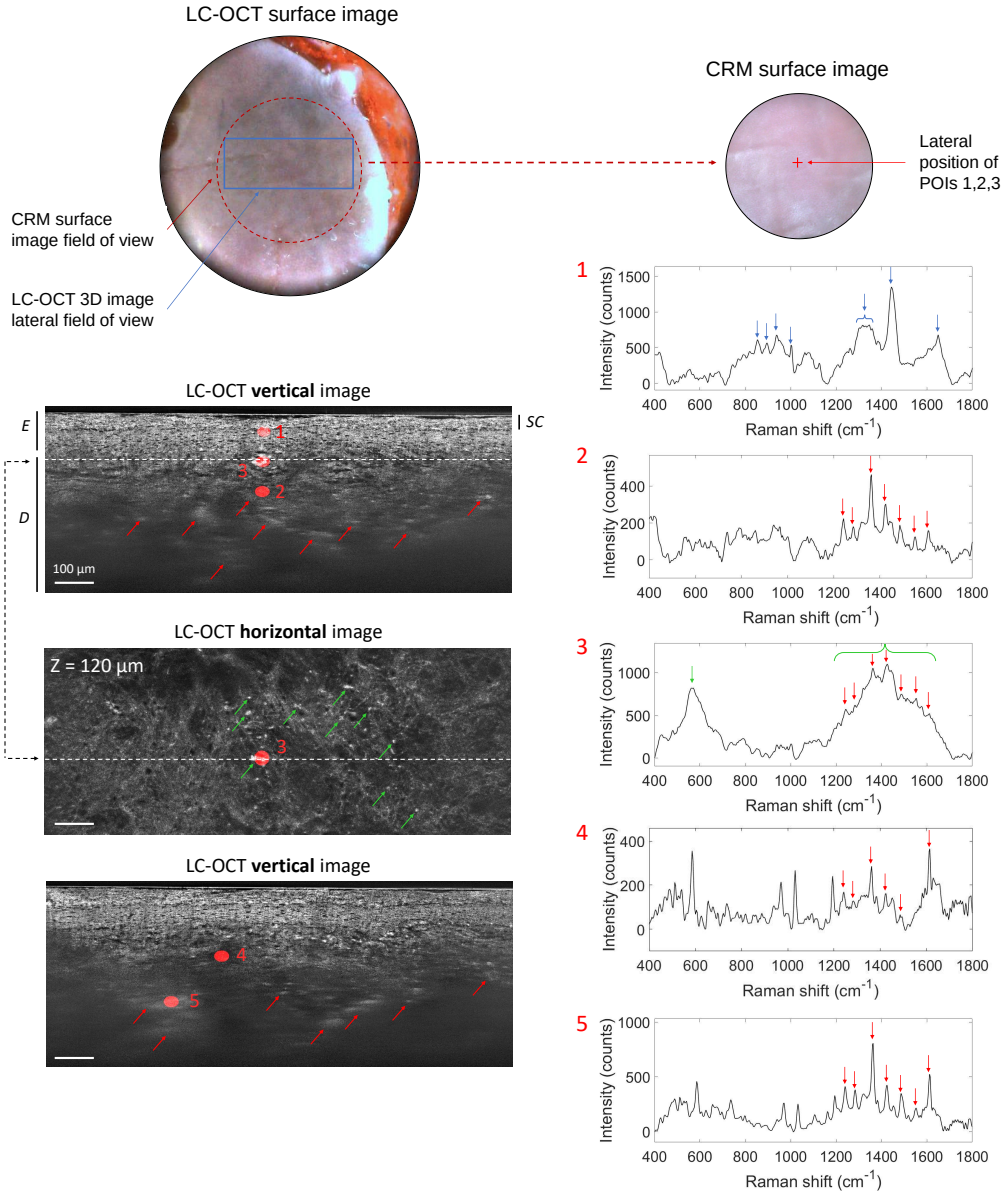

Fig. 7. 3D LC-OCT image (vertical and horizontal views) of a human biopsy taken within the red dye area of a multicolored tattoo, with associated Raman spectra obtained from CRM for five POIs identified in the 3D LC-OCT image and materialized by red ellipsoids. The dotted line on the horizontal image shows the position of the vertical image above regarding the horizontal plane of the 3D image, and vice-versa. The depth Z of the horizontal image is indicated with respect to the skin surface. The different superficial layers of the skin are visualized: the epidermis (E), including the stratum corneum (SC), and the dermis (D). On the LC-OCT images, red arrows point bright areas containing tattoo ink and green arrows show bright particles observed near the dermal-epidermal junction. On the Raman spectra, blue arrows depict Raman bands corresponding to the epidermis and red arrows show Raman peaks assigned to red ink. The green arrow and bracket represent the main Raman bands associated to bright particles observed near the dermal-epidermal junction in the 3D LC-OCT image. Surface images provided by the LC-OCT and CRM devices are also shown.

Biomedical Optics EXPRESS

towards the macrophage hypothesis, which demonstrate the complementarity of LC-OCT and CRM modalities.

Table 1 gathers the main observations made on the red-colored tattoo biopsy. To summarize, LC-OCT-CRM co-localization revealed the presence of red tattoo ink in diffuse bright areas of the dermis. CRM allowed identification of tattoo ink and provided information on its abundance in different areas of the dermis. Small bright structures of unknown nature were spotted near the dermal-epidermal junction using LC-OCT cellular resolution images and analyzed with CRM. CRM provided a better characterization of these structures, which morphology alone do not allow a clear identification, causing potential ambiguity. All these findings demonstrate the strong interest of coupling these two modalities operating at the cellular level.

Table 1. Summary of morphological and biochemical findings obtained on the red-colored tattoo biopsy. Selected Raman peaks refer only to Raman peaks used for biochemical assignment [34, 63, 64, 68–72].

POI	Depth	LC-OCT morphological features	Selected Raman peaks	Assignment
1	45 µm	Epidermal cells (keratinocytes)	852, 895, 936, 1001, 1300-1350, 1443, 1650 cm^{-1}	Epidermis [63]
2	200 µm	Diffuse bright area in the dermis	1239, 1284, 1360, 1422, 1486, 1550, 1612 cm^{-1}	Azo-type red pigment of tattoo ink [34, 64]
3	120 µm	Hyper-reflective particle with irregular shape (40 µm in size) near the dermal-epidermal junction	565, 1200-1650 cm^{-1}	Inflammatory cell (macrophage) [68–72]
4	185 µm	Dermal tissue	1239, 1284, 1360, 1422, 1486, 1550, 1612 cm^{-1}	Red pigment of tattoo ink in low amount
5	305 µm	Diffuse bright area in the dermis	1239, 1284, 1360, 1422, 1486, 1550, 1612 cm^{-1}	Red pigment of tattoo ink in higher amount compared to POI 4

3.2. Biopsy 2: black-colored tattoo

The second sample analyzed is a biopsy of tattoo executed with an unknown black ink. Figure 8 gathers results from co-localization experiments on this biopsy. The 3D LC-OCT image was acquired directly in the dermis due to the positioning of the biopsy in the sample holder. The image shows collagen and elastin fibers constituting the dermis, as well as hypo-reflective areas where light is completely attenuated and no signal visible in the 3D LC-OCT image. Three POIs were targeted and analyzed with CRM within this 3D image. POI 1 is located in a region including well-defined dermal fibers at 20 µm depth; POI 2 was chosen in a relatively small dark area at 80 µm depth and POI 3 in a vast dark region at 225 µm depth.

As expected, the spectrum of POI 1 clearly shows Raman bands related to skin dermis only, with major bands at 815, 853, 884, 939, 1001, 1250-1340, 1452 and 1659 cm^{-1} (blue arrows) [63]. The Raman spectrum of POI 2 shows two broad bands centered at 1320 and 1600 cm^{-1} (black arrows), with additional sharps peaks at 585, 1032 and 1194 cm^{-1} common to the spectra of POIs 4 and 5 of the red-colored tattoo sample (Fig. 7). Investigations are still required to identify those peaks. The two large bands around 1320 and 1600 cm^{-1} are assigned to amorphous carbon and are typical of a carbon black-based pigment [34,36]. This type of pigment was identified

Biomedical Optics EXPRESS

as being related to tattooed skin inflammatory reactions [58] or having an adjuvant effect [61], which supports the hypothesis of the reaction to black tattoo being involved in the development of sarcoidosis. POI 3, located deeper in a broad black region, also exhibits the Raman signature of the carbon black pigment, but with a lower intensity due to light scattering and absorption with depth.

Table 2 resumes the main findings obtained on the black-colored tattoo biopsy. LC-OCT-CRM co-localization allowed to identify the black tattoo ink in the hypo-reflective areas of the dermis, in contrast to the previous red pigment which appeared hyper-reflective. CRM allowed identification of the black pigment type (carbon black) used in the ink, despite the absence of signal in ink-containing areas of the 3D LC-OCT image. The pigment could be identified down to 225 µm depth with CRM, emphasizing the value of CRM for deep tattoo ink identification.

Table 2. Summary of morphological and biochemical findings obtained on the black-colored tattoo biopsy. Selected Raman peaks refer only to Raman peaks used for biochemical assignment [34,36, 63].

POI	Depth	LC-OCT morphological features	Selected Raman peaks	Assignment
1	20 µm	Well-defined dermal fibers	815, 853, 884, 939, 1001, 1250-1340, 1452, 1659 cm^{-1}	Dermis [63]
2	80 µm	Hypo-reflective area in the dermis	Broad bands centered at 1320, 1600 cm^{-1}	Carbon-black pigment of tattoo ink [34, 36]
3	225 µm	Hypo-reflective area in the dermis	Broad bands centered at 1320, 1600 cm^{-1}	Carbon-black pigment of tattoo ink [34, 36]

3.3. Biopsy 3: fulguration-induced tattoo

Lastly, we applied the co-localization approach to the biopsy of fulguration-induced tattoo. As for the black-colored tattoo biopsy, LC-OCT acquisition was performed directly in the dermis. The biopsy includes large dark roundish particles from 20 to 100 µm in diameter and small bright particles from a few to ~ 40 µm in diameter. These particles were assumed to originate from the melting of silver contained in the patient's necklace during the light strike. Four POIs were targeted within a 3D LC-OCT image and analyzed with CRM. Results are given in Fig. 9. POI 1 was chosen 50 µm deep in the dermis; POI 2 spots a large dark roundish particle located underneath POI 1, at 130 µm depth; POIs 3 and 4 both target small (~ 20 µm in size) bright particles located 5 µm deep.

To ease the visualization of the selected Raman peaks used for chemical identification, we have voluntarily set different wavenumber ranges for each POI in Fig. 9. Raman spectrum of POI 1 including dermal tissue, show the main Raman bands of the dermis, highlighted by dark blue arrows [63]. In comparison, the spectrum of POI 2, targeting a dark roundish particle, show no peak corresponding to the dermis but some peaks around 258, 357, 429, 530-670, 775, 845 cm^{-1}. The spectrum of POI 4, targeting a small (~ 20 µm in size) bright particle, exhibits a spectrum similar to the one of POI 2. This observation suggests that both particles, despite having different morphological features, are likely composed of a similar material. The identification of this material is tough. The patient's necklace was assumed to be mainly composed of silver [62] but silver, as all pure metals, is not a Raman-active material [73], but is often used as Raman signal enhancer in surface-enhanced Raman spectroscopy [74]. Nevertheless, according to previous work, a few bands in the spectra of POIs 2 and 4, depicted by light blue arrows, seem to be found in the spectra of silver containing materials. The 258 cm^{-1} shift might be assigned to C-O-Ag

Biomedical Optics EXPRESS

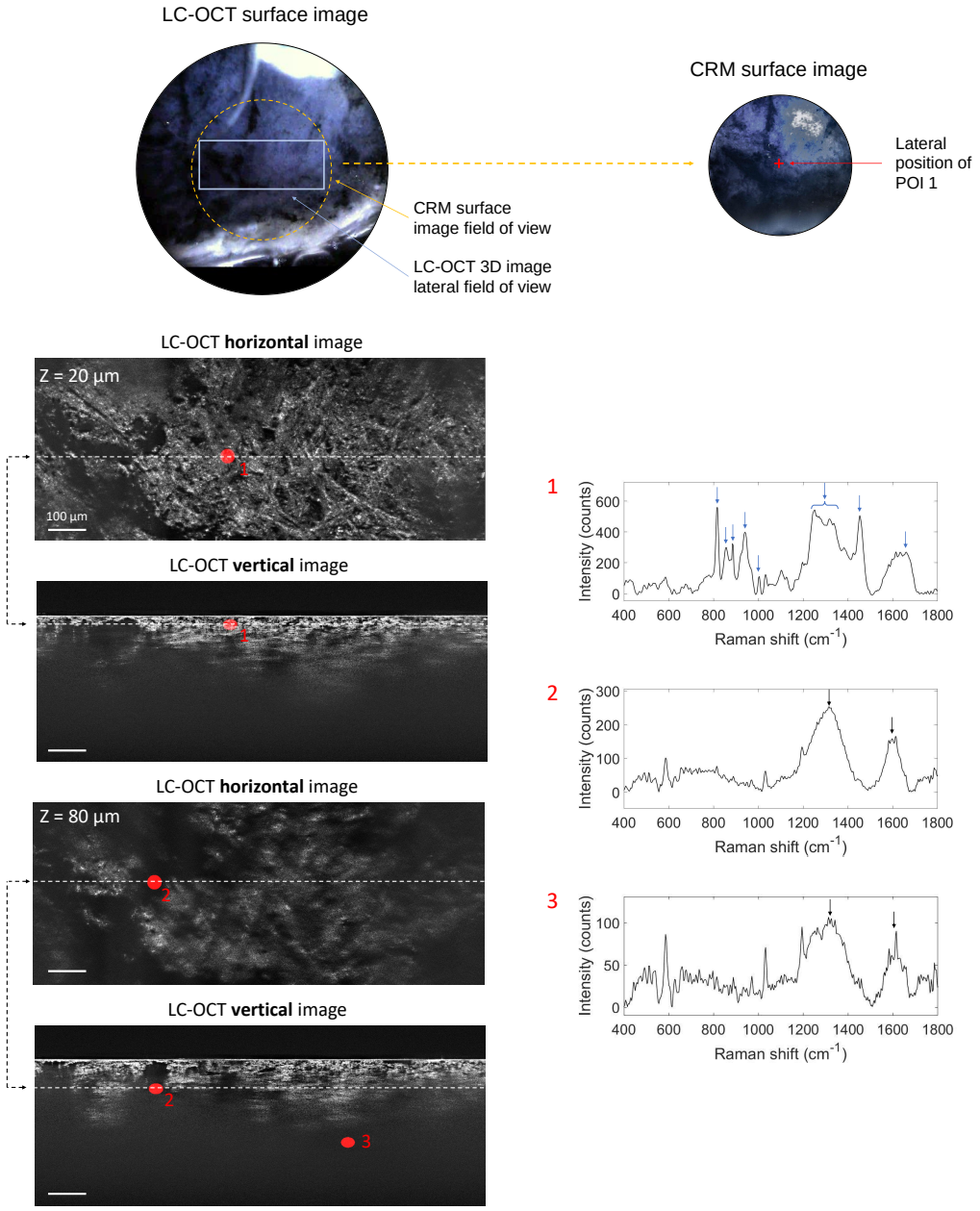

Fig. 8. 3D LC-OCT image (orthogonal views) of a biopsy of a black-colored tattoo, with associated Raman spectra obtained from CRM for three POIs identified in the 3D LC-OCT image and materialized by red ellipsoids. The dotted lines on the horizontal images show the position of the vertical image below regarding the horizontal plane of the 3D image, and vice-versa. The depth Z of the horizontal image is indicated with respect to the skin surface. Blue arrows on Raman spectra depict Raman bands corresponding to dermis and black arrows show Raman bands assigned to the black ink. Surface images provided by the LC-OCT and CRM devices are also shown.

Biomedical Optics EXPRESS

bond [75] or silver oxide Ag_2O [76]. The 429 cm^{-1} band was reported in the spectrum of AgO [77]. These findings are thus coherent with the initial assumption that the necklace is composed of silver or silver-derived materials. The 258 cm^{-1} peak could also be assigned to corrosion products of silver/copper alloys [78], which could also be a potential interpretation since copper is often associated to silver in jewelry and corrosion might have occurred during light strike. The other Raman peaks in the spectra of POIs 2 and 4 have not been identified yet. Other particles were found to be composed of another material, as shown by the spectrum of POI 3. Although targeting a bright small particle of about 20 µm in size and morphologically similar to POI 4, POI 3 exhibits a different spectrum, with two bands at 446 and 611 cm^{-1} revealing the presence of TiO_2 in its rutile form (green arrows) [56]. Titanium is a metal used in jewelry because it has properties of lightness, corrosion resistance and hypoallergenicity. It can be covered with a thin coating of titanium oxide to eventually protect it, which may explain the presence of TiO_2 in the biopsy.

Table 3 resumes the main results obtained on the fulguration-induced tattoo biopsy. In summary, LC-OCT-CRM co-localization allowed to spot foreign body particles in 3D in the sample using LC-OCT imaging, and to analyze their chemical composition using CRM. The high accuracy of co-localization combined to the cellular-resolution of LC-OCT allowed to target particles down to 20 µm in size. Particles of different materials (silver-derived materials, TiO_2) were identified with CRM despite identical morphological features in the LC-OCT image. On the other hand, particles with different morphological features could be identified as being in fact composed of a similar material. Thus, the analysis of this fulguration-induced tattoo biopsy, although complex, demonstrates once again the complementarity of the two modalities at cellular-level, each bringing benefit to the other.

Table 3. Summary of morphological and biochemical findings obtained on the fulguration-induced tattoo biopsy. Selected Raman peaks refer to Raman peaks used for biochemical assignment [56, 63, 75–78].

POI	Depth	LC-OCT morphological features	Selected Raman peaks	Assignment
1	50 µm	Dermal fibers	856, 880, 936, 1001, 1240-1380, 1450, 1664 cm^{-1}	Dermis [63]
2	125 µm	Large (80 µm in size) dark roundish particle in the dermis	258, 429 cm^{-1}	Silver-derived materials: C-O-Ag bond, Ag_2O, AgO, Cu–Ag alloys [75–78]
3	5 µm	Small (20 µm in size) bright particle in the dermis	446, 611 cm^{-1}	Titanium dioxide TiO_2 [56]
4	5 µm	Small (20 µm in size) bright particle in the dermis	258, 429 cm^{-1}	Silver-derived materials: C-O-Ag bond, Ag_2O, AgO, Cu–Ag alloys [75–78]

Biomedical Optics EXPRESS

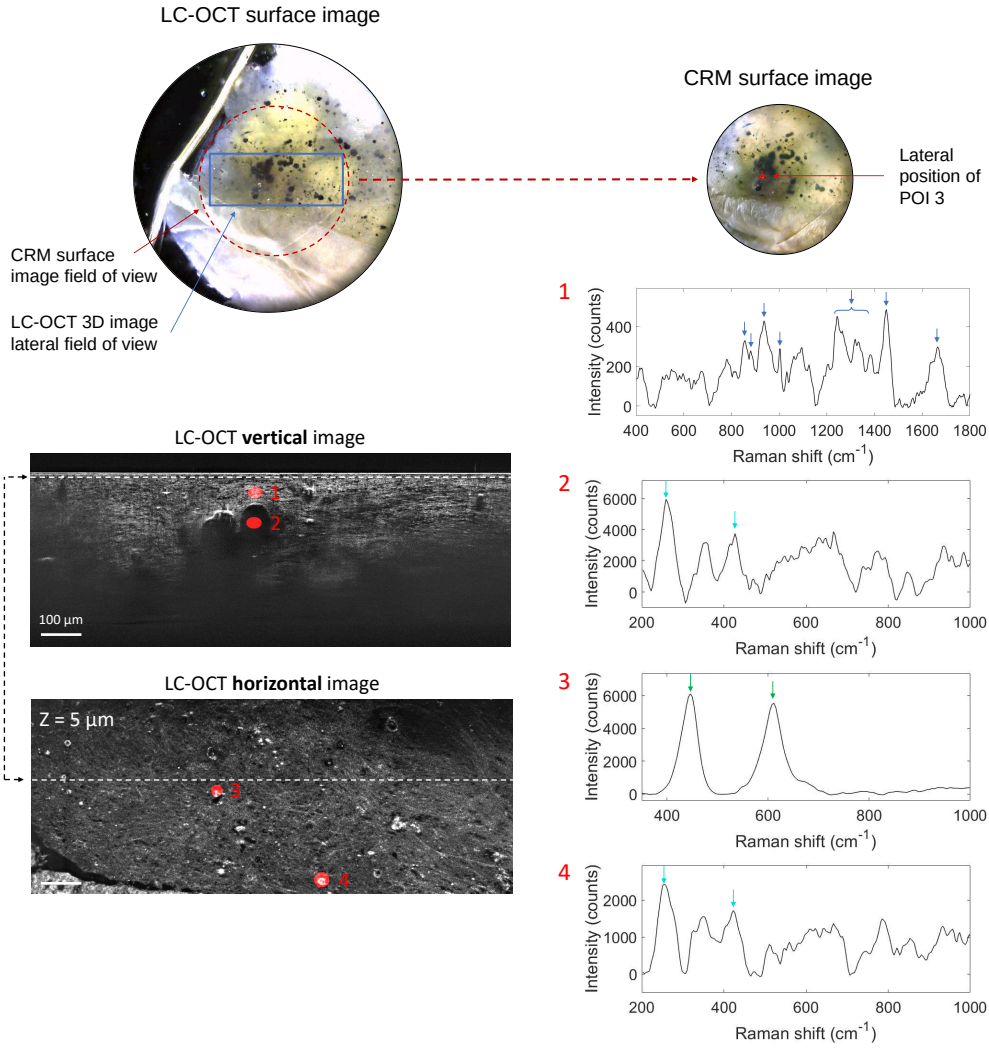

Fig. 9. 3D LC-OCT image (orthogonal views) of a biopsy of a fulguration-induced tattoo, with associated Raman spectra obtained from CRM for four POIs identified in the 3D LC-OCT image and materialized by red ellipsoids. The dotted line on the horizontal image shows the position of the vertical image above regarding the horizontal plane of the 3D image, and vice-versa. The depth Z of the horizontal image is indicated with respect to the skin surface. Dark blue arrows on Raman spectra depict Raman bands corresponding to dermis, light blue arrows correspond to main bands of hypothetical silver-derived materials and green arrows depict the two Raman peaks assigned to TiO_2. Surface images provided by the LC-OCT and CRM devices are also shown.

Biomedical Optics EXPRESS

4. Summary and conclusion

We have developed a method to co-localize data acquired by separate LC-OCT and CRM devices. The method allows acquisition of Raman spectra at specific locations targeted in a 3D LC-OCT image, with an accuracy of ± 20 µm. The co-localization relies on the use of a specific sample holder that can be positioned under each device with high repeatability and of a coordinate-based calibration between the two devices using two independent 3D translation stages. The LC-OCT-CRM co-localization method was applied to morpho-molecular characterization of tattoo biopsies, complementary to previously reported examinations [57,62]. In the three biopsies, co-localization provided LC-OCT with a new level of characterization of the skin, bringing local molecular information precisely located in a 3D image: presence and amount of tattoo ink in specific regions of the samples, identification of ink chemical composition, identification of inflammatory cells and foreign bodies of different materials, which helped to clear ambiguities due to their morphological appearance in the image. In addition, our co-localization approach provides CRM with high resolution imaging guidance, which ensures that the desired micro-structures (such as inflammatory cells of the red dye tattoo biopsy) have effectively been targeted with CRM. Identification of micro-structures to be analyzed with CRM is greatly facilitated by both 2D horizontal and vertical LC-OCT imaging modes, allowing real-time 3D visualization of a sample. The application example on skin tattoos demonstrates that the combination of LC-OCT and CRM provides better characterization of skin samples and allows a better use and interpretation of each modality. A summary of the benefits provided by both LC-OCT and CRM modalities on each biopsy is given in Table 4.

Table 4. Summary of the benefits provided by the combination of LC-OCT and CRM for the three biopsies studied.

Biopsy	Benefits of LC-OCT	Benefits of CRM
Red-colored tattoo	3D location of tattoo ink in the bright areas of the dermis; targeting of cellular-level structures	Identification of the red tattoo pigment type and information on the amount of pigment in-depth; identification of inflammatory cells
Black-colored tattoo	3D location of tattoo ink in hypo-reflective areas of the dermis	Identification of the black pigment type in-depth, despite absorption
Fulguration-induced tattoo	Targeting of cellular-level foreign bodies	Differentiation of materials with similar morphological aspects

The reported co-localization procedure has several limitations. The procedure is relatively long since it needs a calibration step (duration of ~ 2h); it also requires the operator to read and record the coordinates on the manual XYZ stage and to manually displace the sample-holder from the LC-OCT to the CRM devices, which is time-consuming. In terms of performance, the accuracy of our co-localization method (± 20 µm) may be insufficient to target structures at the micrometer scale. Furthermore, tattoo biopsies were optimal samples to demonstrate the value of our co-localization procedure, because the Raman signature of tattoo ink is distinct from that of the skin and intense compared to the skin, allowing the Raman signal to be probed down to a depth of ~ 300 µm. For future applications such as the analysis of suspicious skin lesions, one limitation could be the penetration depth of CRM.

In future technical implementations, the co-localization procedure could be automatized to simplify its use. LC-OCT and CRM systems could be integrated on a single platform, mounted on a XYZ motorized stage for translating the sample holder from the LC-OCT to the CRM device and automatically recording XYZ coordinates from the software associated to the motorized stage.

Biomedical Optics EXPRESS

The automated platform would make the co-localization procedure faster and more practical to implement in a clinical setting. It could also allow to reach a better co-localization accuracy using a smaller motor pitch than the one of manual stages. Moreover, *in vivo* co-localization could be investigated based on the registration of the surface images of LC-OCT and CRM set-ups, using identical morphological features identified with both images on the surface of the sample. Finally, since the co-localization approach does not require any hardware modification of each modality, it could eventually be extended to different couplings involving other optical techniques such as fluorescence microscopy, two-photon microscopy and autofluorescence spectroscopy. The technical proof of concept and the practical interest of co-localized measurements using different and complementary modalities, demonstrated in this paper, suggest that this approach has the potential to open up to a wide range of applications in dermatology, where the combination of morphological and molecular information at the cellular level is of interest, including for skin cancer diagnosis and research.

Funding. Université Paris-Saclay; Association Nationale de la Recherche et de la Technologie.

Acknowledgments. The authors wish to acknowledge the whole team of engineers at DAMAE Medical for technical support.

Disclosures. Léna Waszczuk and Dr. Jonas Ogien are engineers employed by DAMAE Medical. Pr. Jean-Luc Perrot is a dermatologist at the University Hospital of Saint-Etienne. Pr. Arnaud Dubois invented the patent of the LC-OCT technology and is co-founder of DAMAE Medical.

Data availability. Data underlying the results presented in this paper may be obtained from the authors upon reasonable request.

Supplemental document. See Supplement 1 for supporting content.

References

1. A. Dubois, O. Levecq, H. Azimani, D. Siret, A. Barut, M. Suppa, V. del Marmol, J. Malvehy, E. Cinotti, P. Rubegni, and J.-L. Perrot, "Line-field confocal optical coherence tomography for high-resolution noninvasive imaging of skin tumors," J. Biomed. Opt. **23**(10), 1 (2018).
2. A. Dubois, O. Levecq, H. Azimani, A. Davis, J. Ogien, D. Siret, and A. Barut, "Line-field confocal time-domain optical coherence tomography with dynamic focusing," Opt. Express **26**(26), 33534 (2018).
3. A. Davis, O. Levecq, H. Azimani, D. Siret, and A. Dubois, "Simultaneous dual-band line-field confocal optical coherence tomography: application to skin imaging," Biomed. Opt. Express **10**(2), 694–706 (2019).
4. J. Ogien, A. Daures, M. Cazalas, J. L. Perrot, and A. Dubois, "Line-field confocal optical coherence tomography for three-dimensional skin imaging," Front. Optoelectron. **13**(4), 381–392 (2020).
5. J. Ogien, O. Levecq, H. Azimani, and A. Dubois, "Dual-mode line-field confocal optical coherence tomography for ultrahigh-resolution vertical and horizontal section imaging of human skin in vivo," Biomed. Opt. Express **11**(3), 1327 (2020).
6. M. Pedrazzani, J. Breugnot, P. Rouaud-Tinguely, M. Cazalas, A. Davis, S. Bordes, A. Dubois, and B. Closs, "Comparison of line-field confocal optical coherence tomography images with histological sections: Validation of a new method for in vivo and non-invasive quantification of superficial dermis thickness," Ski. Res. Technol. **26**(3), 398–404 (2020).
7. C. Ruini, S. Schuh, E. Sattler, and J. Welzel, "Line-field confocal optical coherence tomography-Practical applications in dermatology and comparison with established imaging methods," Ski. Res. Technol. **27**(3), 340–352 (2021).
8. J. Chauvel-Picard, V. Bérot, L. Tognetti, C. Orte Cano, M. Fontaine, C. Lenoir, J. Pérez-Anker, S. Puig, A. Dubois, S. Forestier, J. Monnier, R. Jdid, G. Cazorla, M. Pedrazzani, A. Sanchez, S. Fischman, P. Rubegni, V. del Marmol, J. Malvehy, E. Cinotti, J. L. Perrot, and M. Suppa, "Line-field confocal optical coherence tomography as a tool for three-dimensional in vivo quantification of healthy epidermis: A pilot study," J. Biophotonics **15**(2), e202100236 (2022).
9. M. Suppa, M. Fontaine, G. Dejonckheere, E. Cinotti, O. Yélamos, G. Diet, L. Tognetti, M. Miyamoto, C. Orte Cano, J. Perez-Anker, V. Panagiotou, A. Trepant, J. Monnier, V. Berot, S. Puig, P. Rubegni, J. Malvehy, J. Perrot, and V. Marmol, "Line-field confocal optical coherence tomography of basal cell carcinoma: a descriptive study," J. Eur. Acad. Dermatol. Venereol. **35**(5), 1099–1110 (2021).
10. C. Ruini, S. Schuh, C. Gust, B. Kendziora, L. Frommherz, L. E. French, D. Hartmann, J. Welzel, and E. Sattler, "Line-field optical coherence tomography: in vivo diagnosis of basal cell carcinoma subtypes compared with histopathology," Clin. Exp. Dermatol. **46**(8), 1471–1481 (2021).
11. E. Cinotti, L. Tognetti, A. Cartocci, A. Lamberti, S. Gherbassi, C. Orte Cano, C. Lenoir, G. Dejonckheere, G. Diet, M. Fontaine, M. Miyamoto, J. Perez-Anker, V. Solmi, J. Malvehy, V. Marmol, J. L. Perrot, P. Rubegni, and M. Suppa,

Biomedical Optics EXPRESS

"Line-field confocal optical coherence tomography for actinic keratosis and squamous cell carcinoma: a descriptive study," Clin. Exp. Dermatol. **46**(8), 1530–1541 (2021).
12. C. Lenoir, E. Cinotti, L. Tognetti, C. Orte Cano, G. Diet, M. Miyamoto, L. Rocq, A. Trépant, J. Perez-Anker, S. Puig, J. Malvehy, P. Rubegni, J. Perrot, V. Marmol, and M. Suppa, "Line-field confocal optical coherence tomography of actinic keratosis: a case series," J. Eur. Acad. Dermatol. Venereol. **35**, 1–3 (2021).
13. D. W. Shipp, F. Sinjab, and I. Notingher, "Raman spectroscopy: techniques and applications in the life sciences," Adv. Opt. Photonics **9**(2), 315–428 (2017).
14. L. Chrit, P. Bastien, B. Biatry, J.-T. Simonnet, A. Potter, A. M. Minondo, F. Flament, R. Bazin, G. D. Sockalingum, F. Leroy, M. Manfait, and C. Hadjur, "In vitro and in vivo confocal Raman study of human skin hydration: Assessment of a new moisturizing agent, pMPC," Biopolymers **85**(4), 359–369 (2007).
15. M. Egawa and H. Iwaki, "In vivo evaluation of the protective capacity of sunscreen by monitoring urocanic acid isomer in the stratum corneum using Raman spectroscopy," Ski. Res. Technol. **14**(4), 410–417 (2008).
16. M. G. Tosato, R. S. Alves, E. A. dos Santos, L. Raniero, P. F. Menezes, K. M. Belletti, C. E. O. Praes, and A. A. Martin, "Raman spectroscopic investigation of the effects of cosmetic formulations on the constituents and properties of human skin," Photomed. Laser Surg. **30**(2), 85–91 (2012).
17. S. Tfaili, G. Josse, J.-F. Angiboust, M. Manfait, and O. Piot, "Monitoring caffeine and resveratrol cutaneous permeation by confocal Raman microspectroscopy," J. Biophotonics **7**(9), 676–681 (2014).
18. L. dos Santos, C. A. T. Soto, P. P. Favero, and A. A. Martin, "In vivo confocal Raman spectroscopy study of the vitamin A derivative perfusion through human skin," in *Biomedical Vibrational Spectroscopy 2016: Advances in Research and Industry*, vol. 9704 A. Mahadevan-Jansen and W. Petrich, eds., International Society for Optics and Photonics (SPIE, 2016), pp. 90–93.
19. M. Essendoubi, C. Gobinet, R. Reynaud, J. F. Angiboust, M. Manfait, and O. Piot, "Human skin penetration of hyaluronic acid of different molecular weights as probed by Raman spectroscopy," Ski. Res. Technol. **22**(1), 55–62 (2016).
20. U. Lopez-Gonzalez, A. Casey, and H. J. Byrne, "Monitoring the biochemical changes occurring to human keratinocytes exposed to solar radiation by Raman spectroscopy," J. Biophotonics **14**, e202000337 (2021).
21. G. Kourbaj, S. Bielfeldt, M. Seise, and K. Wilhelm, "Measurement of dermal water content by confocal RAMAN spectroscopy to investigate intrinsic aging and photoaging of human skin in vivo," Ski. Res. Technol. **27**(3), 404–413 (2021).
22. R. Boitor, C. de Wolf, F. Weesie, D. W. Shipp, S. Varma, D. Veitch, A. Wernham, A. Koloydenko, G. Puppels, T. Nijsten, H. C. Williams, P. Caspers, and I. Notingher, "Clinical integration of fast Raman spectroscopy for Mohs micrographic surgery of basal cell carcinoma," Biomed. Opt. Express **12**(4), 2015–2026 (2021).
23. X. Feng, M. C. Fox, J. S. Reichenberg, F. C. P. S. Lopes, K. R. Sebastian, M. K. Markey, and J. W. Tunnell, "Biophysical basis of skin cancer margin assessment using Raman spectroscopy," Biomed. Opt. Express **10**(1), 104–118 (2019).
24. J. Choi, J. Choo, H. Chung, D.-G. Gweon, J. Park, H. J. Kim, S. Park, and C.-H. Oh, "Direct observation of spectral differences between normal and basal cell carcinoma (BCC) tissues using confocal Raman microscopy," Biopolymers **77**(5), 264–272 (2005).
25. A. Nijssen, T. C. Bakker Schut, P. J. Caspers, G. J. Puppels, F. Heule, M. H. Neumann, and D. P. Hayes, "Discriminating basal cell carcinoma from its surrounding tissue by raman spectroscopy," J. Invest. Dermatol. **119**(1), 64–69 (2002).
26. C. A. Lieber, S. K. Majumder, D. Billheimer, D. L. Ellis, and A. Mahadevan-Jansen, "Raman microspectroscopy for skin cancer detection in vitro," J. Biomed. Opt. **13**(2), 024013 (2008).
27. C. Lieber and A. Mahadevan-Jansen, "Development of a handheld Raman microspectrometer for clinical dermatologic applications," Opt. Express **15**(19), 11874 (2007).
28. A. C. Terentis, S. A. Fox, S. J. Friedman, and E. S. Spencer, "Confocal Raman microspectroscopy discriminates live human metastatic melanoma and skin fibroblast cells," J. Raman Spectrosc. **44**(9), 1205–1216 (2013).
29. P. J. Cosme, J. Ye, S. Sears, E. P. Wojcikiewicz, and A. C. Terentis, "Label-free confocal Raman mapping of transportan in melanoma cells," Mol. Pharmaceutics **15**(3), 851–860 (2018).
30. M. A. Short, H. Lui, D. McLean, H. Zeng, A. Alajlan, and X. K. Chen, "Changes in nuclei and peritumoral collagen within nodular basal cell carcinomas via confocal micro-Raman spectroscopy," J. Biomed. Opt. **11**(3), 034004 (2006).
31. H. Wang, N. Huang, J. Zhao, H. Lui, M. Korbelik, and H. Zeng, "Depth-resolved in vivo micro-Raman spectroscopy of a murine skin tumor model reveals cancer-specific spectral biomarkers," J. Raman Spectrosc. **42**(2), 160–166 (2011).
32. X. Zhang, F. Yu, J. Li, D. Song, H. Li, K. Wang, Q. He, and S. Wang, "Investigation on the cancer invasion and metastasis of skin squamous cell carcinoma by Raman spectroscopy," Molecules **24**(11), 2059 (2019).
33. X. Feng, A. J. Moy, H. T. M. Nguyen, J. Zhang, M. C. Fox, K. R. Sebastian, J. S. Reichenberg, M. K. Markey, and J. W. Tunnell, "Raman active components of skin cancer," Biomed. Opt. Express **8**(6), 2835 (2017).
34. B. J. Yakes, T. J. Michael, M. Perez-Gonzalez, and B. P. Harp, "Investigation of tattoo pigments by Raman spectroscopy," J. Raman Spectrosc. **48**(5), 736–743 (2017).
35. E. M. Bauer, T. De Caro, P. Tagliatesta, and M. Carbone, "Unraveling the real pigment composition of tattoo inks: the case of bi-components phthalocyanine based greens," Dyes Pigm. **167**, 225–235 (2019).

Biomedical Optics EXPRESS

36. M. E. Darvin, J. Schleusener, F. Parenz, O. Seidel, C. Krafft, J. Popp, and J. Lademann, "Confocal Raman microscopy combined with optical clearing for identification of inks in multicolored tattooed skin in vivo," Analyst (Cambridge, U. K.) **143**(20), 4990–4999 (2018).
37. K. Hutton Carlsen, M. Køcks, M. Sepehri, and J. Serup, "Allergic reactions in red tattoos: Raman spectroscopy for 'fingerprint' detection of chemical risk spectra in tattooed skin and culprit tattoo inks," Ski. Res. Technol. **22**(4), 460–469 (2016).
38. S. Persechino, C. Toniolo, A. Ciccola, I. Serafini, A. Tammaro, P. Postorino, F. Persechino, and M. Serafini, "A new high-throughput method to make a quality control on tattoo inks," Spectrochim. Acta, Part A **206**, 547–551 (2019).
39. C. A. Patil, H. Kirshnamoorthi, D. L. Ellis, T. G. van Leeuwen, and A. Mahadevan-Jansen, "A clinical instrument for combined raman spectroscopy-optical coherence tomography of skin cancers," Lasers Surg. Med. **43**(2), 143–151 (2011).
40. A. Varkentin, M. Mazurenka, E. Blumenröther, L. Behrendt, S. Emmert, U. Morgner, M. Meinhardt-Wollweber, M. Rahlves, and B. Roth, "Trimodal system for in vivo skin cancer screening with combined optical coherence tomography-Raman and colocalized optoacoustic measurements," J. Biophotonics **11**(6), e201700288 (2018).
41. V. P. Zakharov, I. A. Bratchenko, S. V. Kozlov, A. A. Moryatov, D. V. Kornilin, O. O. Myakinin, and D. N. Artemyev, "Advances in tumor diagnosis using OCT and Raman spectroscopy," in *Biophotonics: Photonic Solutions for Better Health Care IV*, vol. 9129 J. Popp, V. V. Tuchin, D. L. Matthews, F. S. Pavone, and P. Garside, eds., International Society for Optics and Photonics (SPIE, 2014), pp. 58–64.
42. V. P. Zakharov, I. A. Bratchenko, D. N. Artemyev, O. O. Myakinin, D. V. Kornilin, S. V. Kozlov, and A. A. Moryatov, "Comparative analysis of combined spectral and optical tomography methods for detection of skin and lung cancers," J. Biomed. Opt. **20**(2), 025003 (2015).
43. K. Egodage, S. Dochow, T. Bocklitz, O. Chernavskaia, C. Matthaeus, M. Schmitt, and J. Popp, "The combination of optical coherence tomography and Raman spectroscopy for tissue characterization," J. Biomed. Photonics Eng. **72**, 169–177 (2015).
44. M. Mazurenka, L. Behrendt, M. Meinhardt-Wollweber, U. Morgner, and B. Roth, "Development of a combined OCT-Raman probe for the prospective in vivo clinical melanoma skin cancer screening," Rev. Sci. Instrum. **88**(10), 105103 (2017).
45. P. J. Caspers, G. W. Lucassen, H. A. Bruining, and G. J. Puppels, "Automated depth-scanning confocal Raman microspectrometer for rapidin vivo determination of water concentration profiles in human skin," J. Raman Spectrosc. **31**(8-9), 813–818 (2000).
46. P. J. Caspers, H. A. Bruining, G. J. Puppels, G. W. Lucassen, and E. A. Carter, "In Vivo Confocal Raman Microspectroscopy of the Skin: Noninvasive Determination of Molecular Concentration Profiles," J. Invest. Dermatol. **116**(3), 434–442 (2001).
47. H. Wang, A. M. D. Lee, H. Lui, D. I. McLean, and H. Zeng, "A Method for accurate in vivo micro-Raman spectroscopic measurements under guidance of advanced microscopy imaging," Sci. Rep. **3**(1), 1890 (2013).
48. X. Feng, M. C. Fox, J. S. Reichenberg, F. C. P. S. Lopes, K. R. Sebastian, A. K. Dunn, M. K. Markey, and J. W. Tunnell, "Rapid assessment of skin surgical margins using superpixel Raman spectroscopic imaging," in *Molecular-Guided Surgery: Molecules, Devices, and Applications VI*, vol. 11222 S. Gioux, S. L. Gibbs, and B. W. Pogue, eds., International Society for Optics and Photonics (SPIE, 2020), p. 1122205.
49. F. Placzek, E. Cordero Bautista, S. Kretschmer, L. M. Wurster, F. Knorr, G. González-Cerdas, M. T. Erkkilä, P. Stein, Ç. Ataman, G. G. Hermann, K. Mogensen, T. Hasselager, P. E. Andersen, H. Zappe, J. Popp, W. Drexler, R. A. Leitgeb, and I. W. Schie, "Morpho-molecular ex vivo detection and grading of non-muscle-invasive bladder cancer using forward imaging probe based multimodal optical coherence tomography and Raman spectroscopy," Analyst **145**(4), 1445–1456 (2020).
50. I. W. Schie, F. Placzek, F. Knorr, E. Cordero, L. M. Wurster, G. G. Hermann, K. Mogensen, T. Hasselager, W. Drexler, J. Popp, and R. A. Leitgeb, "Morpho-molecular signal correlation between optical coherence tomography and Raman spectroscopy for superior image interpretation and clinical diagnosis," Sci. Rep. **11**(1), 9951 (2021).
51. A. Dubois, "Focus defect and dispersion mismatch in full-field optical coherence microscopy," Appl. Opt. **56**(9), D142–D150 (2017).
52. N. Kourkoumelis, I. Balatsoukas, V. Moulia, A. Elka, G. Gaitanis, and I. Bassukas, "Advances in the in Vivo Raman Spectroscopy of Malignant Skin Tumors Using Portable Instrumentation," Int. J. Mol. Sci. **16**(12), 14554–14570 (2015).
53. J. Schleusener, C. Reble, M. C. Meinke, and J. Helfmann, "Raman spectroscopy for the discrimination of cancerous and normal skin," Photonics & Lasers in Medicine **4**(2), 151–167 (2015).
54. V. V. Tuchin, "Light scattering study of tissues," Phys.-Usp. **40**(5), 495–515 (1997).
55. A. N. Bashkatov, E. A. Genina, V. I. Kochubey, and V. V. Tuchin, "Optical properties of human skin, subcutaneous and mucous tissues in the wavelength range from 400 to 2000 nm," J. Phys. D: Appl. Phys. **38**(15), 2543–2555 (2005).
56. T. Mazza, E. Barborini, P. Piseri, P. Milanik, D. Cattaneo, A. L. Bassi, C. E. Bottani, and C. Ducati, "Raman spectroscopy characterization of tio2 rutile nanocrystals," Phys. Rev. B **75**(4), 045416 (2007).
57. L. Tognetti, S. Ekinde, C. Habougit, E. Cinotti, P. Rubegni, and J. L. Perrot, "Delayed Tattoo Reaction From Red Dye With Overlapping Clinicopathological Features: Examination With High-Frequency Ultrasound and Line-Field Optical Coherence Tomography," Dermatol. Pract. & Concept. **10**, e2020053 (2020).

Biomedical Optics EXPRESS

58. J. Serup, K. Hutton Carlsen, N. Dommershausen, M. Sepehri, B. Hesse, C. Seim, A. Luch, and I. Schreiver, "Identification of pigments related to allergic tattoo reactions in 104 human skin biopsies," Contact Dermatitis **82**(2), 73–82 (2020).
59. K. Hanada, S. Chiyoya, and Y. Katabira, "Systemic sarcoidal reaction in tattoo," Clin. Exp. Dermatol. **10**(5), 479–484 (1985).
60. H. Kushima, Y. Kinoshita, H. Ishii, and M. Fujita, "Tattoo-induced systemic sarcoidosis," BMJ Case Reports **13**(8), e237723 (2020).
61. M. Sepehri, K. Hutton Carlsen, and J. Serup, "Papulo-nodular reactions in black tattoos as markers of sarcoidosis: study of 92 tattoo reactions from a hospital material," Dermatology (Basel, Switz.) **232**(6), 679–686 (2016).
62. E. Cinotti, F. Bruzziches, C. Habougit, V. Berot, L. Tognetti, P. Rubegni, and J. L. Perrot, "Fulguration-induced tattoo," Clin. Exp. Dermatol. **45**(7), 911–912 (2020).
63. A. Tfayli, "Caractérisation structurale et moléculaire de la peau par microspectroscopies optiques vibrationnelles. Applications au diagnostic précoce des tumeurs cutanées et à l'étude de la diffusion de principes actifs à visée thérapeutique," Ph.D. thesis (2007).
64. M. Manso, S. Pessanha, M. Guerra, U. Reinholz, C. Afonso, M. Radtke, H. Lourenço, M. L. Carvalho, and A. G. Buzanich, "Assessment of Toxic Metals and Hazardous Substances in Tattoo Inks Using Sy-XRF, AAS, and Raman Spectroscopy," Biol. Trace Elem. Res. **187**(2), 596–601 (2019).
65. I. Waldmann and F. Vakilzadeh, "Allergische Spättypreaktion auf roten Azofarbstoff in Tätowierungen," Hautarzt **48**(9), 666–670 (1997).
66. S. Gaudron, M.-C. Ferrier-Le Bouëdec, F. Franck, and M. D'Incan, "Azo pigments and quinacridones induce delayed hypersensitivity in red tattoos," Contact Dermatitis **72**(2), 97–105 (2015).
67. I. Steinbrecher, W. Hemmer, and R. Jarisch, "Adverse reaction to the azo dye Pigment Red 170 in a tattoo," J. der Deutschen Dermatol. Gesellschaft **2**, 1007–1012 (2004).
68. P. Guitera, L.-X. L. Li, R. A. Scolyer, and S. W. Menzies, "Morphologic features of melanophages under in vivo reflectance confocal microscopy," Arch. Dermatol. **146**(5), 492–498 (2010).
69. A. Guichard, M. Agozzino, P. Humbert, F. Fanian, A. Elkyat, and M. Ardigò, "Skin rejecting tattoo ink followed, in vivo, by reflectance confocal microscopy Editor," J. Eur. Acad. Dermatol. Venereol. **28**(3), 391–393 (2014).
70. C. Reilly, N. Chuchvara, J. Cucalon, R. Srivastava, and B. K. Rao, "Reflectance confocal microscopy evaluation of pigmented lesions on tattooed skin," Lasers Med. Sci. **36**(5), 1077–1084 (2021).
71. L. Tetard, A. Passian, K. T. Venmar, R. M. Lynch, B. H. Voy, G. Shekhawat, V. P. Dravid, and T. Thundat, "Imaging nanoparticles in cells by nanomechanical holography," Nat. Nanotechnol. **3**(8), 501–505 (2008).
72. L. Tetard, A. Passian, R. H. Farahi, B. H. Voy, and T. Thundat, "Applications of subsurface microscopy," *Methods in Molecular Biology*, **926**, 331–343 (2012).
73. I. R. Lewis and H. Edwards, *Handbook of Raman Spectroscopy* (CRC Press, 2001), 1st ed.
74. B. Brozek-Pluska, M. Kopec, and J. Surmacki, "Surface-enhanced raman spectroscopy analysis of human breast cancer via silver nanoparticles: an examination of fabrication methods," J. Spectrosc. **2018**, 1–8 (2018).
75. I. Martina, R. Wiesinger, and M. Schreiner, "Micro-Raman characterisation of silver corrosion products : instrumental set up and reference," e-Preservation Science **9**, 1–8 (2012).
76. I. Martina, R. Wiesinger, and M. Schreiner, "Micro-Raman investigations of early stage silver corrosion products occurring in sulfur containing atmospheres," J. Raman Spectrosc. **44**(5), 770–775 (2013).
77. G. I. N. Waterhouse, G. A. Bowmaker, and J. B. Metson, "The thermal decomposition of silver (I, III) oxide: A combined XRD, FT-IR and Raman spectroscopic study," Phys. Chem. Chem. Phys. **3**(17), 3838–3845 (2001).
78. T. de Caro, D. Caschera, G. M. Ingo, and P. Calandra, "Micro-Raman innovative methodology to identify Ag-Cu mixed sulphides as tarnishing corrosion products," J. Raman Spectrosc. **47**(7), 852–859 (2016).